Extreme Mechanics Letters 61 (2023) 101981

Contents lists available at ScienceDirect

Extreme Mechanics Letters

journal homepage: www.elsevier.com/locate/eml

Maximizing electro-momentum coupling in generalized 2D Willis Metamaterials

Hai D. Huynh [b], Xiaoying Zhuang [a,b,*], Harold S. Park [c,**], S.S. Nanthakumar [b], Yabin Jin [e], Timon Rabczuk [d,**]

[a] Department of Geotechnical Engineering, College of Civil Engineering, Tongji University, Shanghai, China
[b] Chair of Computational Science and Simulation Technology, Department of Mathematics and Physics, Leibniz University Hannover, Germany
[c] Department of Mechanical Engineering, Boston University, Boston, MA 02215, USA
[d] Institute of Structural Mechanics, Bauhaus-Universität Weimar, Weimar, Germany
[e] School of Aerospace Engineering and Applied Mechanics, Tongji University, Shanghai, China

ARTICLE INFO

Article history:
Received 12 August 2022
Received in revised form 11 December 2022
Accepted 17 February 2023
Available online 24 February 2023

Keywords:
Dynamic homogenization
Elastodynamics
Willis materials
Topology optimization
Asymmetric wave propagation

ABSTRACT

The coupling of momentum to strain in elastic metamaterials, known as the Willis coupling, has been widely studied in recent years for its potential in enabling novel phenomena in wave propagation. More recent work has shown that in piezoelectric composites, the momentum can also be coupled to the electrical stimulus, resulting in a new form of electro-momentum coupling, which offers a new approach to controlling elastic wave phenomena through a non-mechanical stimulus. In this study, we present a topology optimization approach to maximize the electro-momentum coupling in piezoelectric composites, where dynamic homogenization is utilized to obtain the effective mechanical, electrical, and electro-mechanical constitutive relations. We first validate the approach in one-dimension, then demonstrate that the electro-momentum coupling can enable asymmetric wave propagation in two-dimensions, both through mechanical and electrical loadings. This approach can enable the design of piezoelectric composites that support novel wave phenomena that can be excited through non-mechanical means.

1. Introduction

The development of metamaterials in recent years has opened new research directions to simulate waves in acoustics [1,2], optics [3], electromagnetism [4,5], and elastodynamics [6–8]. Of particular interest are the class of Willis metamaterials [9,10], in which momentum is coupled to strain, which were found to enable novel wave phenomena, including cloaking and non-reciprocal wave propagation. Willis metamaterials are obtained using homogenization to connect the effects of microscale heterogeneities to the dynamic macroscale continuum response. One noticeable feature of the dynamic homogenization is the appearance of coupling terms, known as Willis couplings in effective constitutive relations. In particular, there have been various cross-couplings derived to connect strain and momentum in elastodynamics [11–13], pressure and momentum in acoustics [14,15], or electric and magnetic fields in electromagnetism [16,17]. As a generalization of standard material properties, the physical restrictions with respect to reciprocity, causality and passivity must be enforced. These restrictions have developed in elastodynamics by Srivastava et al. [18,19], Haberman et al. [20] and Milton [21], or in elastic and acoustic materials by Achenbach [22]. Successive derivation on passivity is done to show bounds on the Willis response of acoustics [15].

While classical Willis materials have been derived to highlight their novel properties through cross-couplings between strain and velocity, Shmuel and co-workers [23] recently developed a new coupling, in addition to Willis coupling, between the momentum and non-mechanical field. Specifically, they found that the macroscopic momentum for piezoelectric composites can be additionally coupled with the electric field, while the velocity is coupled to the electric displacement as described in Fig. 1, where distinctions and connections to Willis coupling are illustrated. The mathematical restrictions on such effective properties were discussed in Ref. [24], while the authors recently developed a scattering-based homogenization method [25] to analyze elastic waves in 1D piezoelectric Willis materials and to highlight the importance of electro-momentum coupling on their macroscopic description. An alternative homogenization method [26] derived from plane wave expansions was also recently done for

* Corresponding author at: Chair of Computational Science and Simulation Technology, Department of Mathematics and Physics, Leibniz University Hannover, Germany.
** Corresponding authors.
E-mail addresses: zhuang@iop.uni-hannover.de (X. Zhuang), parkhs@bu.edu (H.S. Park), timon.rabczuk@uni-weimar.de (T. Rabczuk).

https://doi.org/10.1016/j.eml.2023.101981
2352-4316/

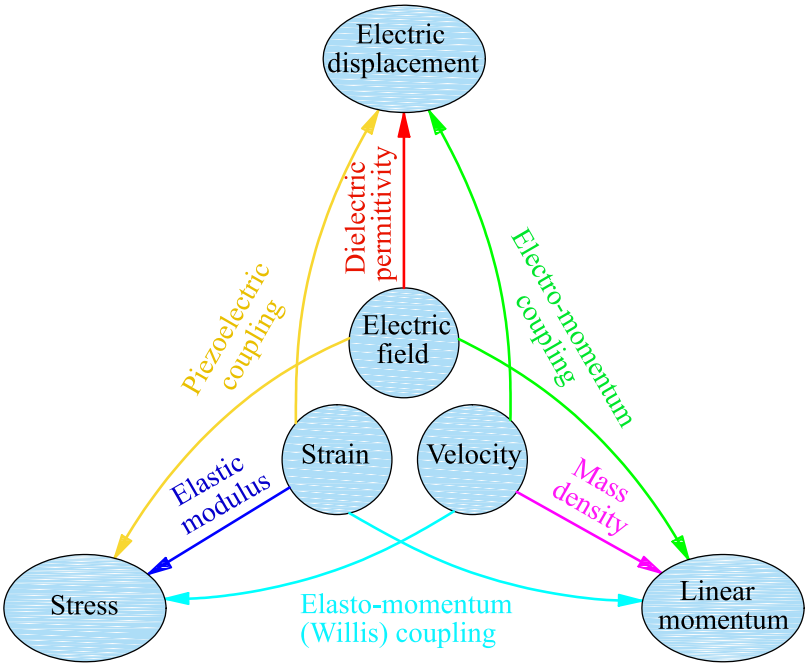

Fig. 1. Diagram of electro-momentum coupling in piezoelectric metamaterials, and its relationship with standard Willis coupling.

quasi-2D generalized Willis materials. The emergence of electro-momentum coupling has recently lead to works on maximizing the coupling coefficient by derivation of theoretical bounds in 2D [27], and by topology optimization in piezoelectric layers [28]. While Shmuel et al. [23] presented an elegant analytical solution for a one-dimensional problem with only mechanical loading, the complexity of the theoretical formulation motivates the development of a computational formulation to enable developing insights into the structure–property relationships that enable maximizing this new electro-momentum coupling, particularly in multiple dimensions. Since the classical Willis coupling has been discovered to handle a nonreciprocal medium for acoustic waves [22,29], elastic waves [30], or to drive asymmetric wave responses [31], it is an open question as to the potential of electro-momentum coupling for similar applications, where due to the emergence of these new couplings in piezoelectric metamaterials, a momentum bias can be produced via electric fields to control elastic waves. Specifically, it is of interest to find material distributions whose the electro-momentum coupling is maximized to produce a sufficiently strong momentum bias.

The objective of the present work is to develop a numerical framework based on the ensemble averaging technique to homogenize periodic piezoelectric media, and to use the resulting effective constitutive relationships to design piezoelectric metamaterials which maximize the electro-momentum coupling. To do so, we develop a genetic algorithm-based topology optimization approach for periodic structures, and use the resulting optimized unit cells to demonstrate asymmetric wave propagation induced by both mechanical and electrical loads in a two-dimensional piezoelectric composite metamaterial.

The paper outline is as follows. Section 2 shows the mathematical model based on the ensemble average to homogenize piezoelectric composites. Fundamental properties of the effective constitutive relations are briefly discussed in this section. In Section 3, a 1D problem is examined to validate the present computational work in comparison with the analytical result proposed by Salomón [23]. For two-dimensional problems, we develop a topology optimization algorithm to maximize the electro-momentum coupling, whose effects on wave propagation we demonstrate through numerical examples.

2. Derivation of the effective electro-mechanical constitutive relationships

In this section, we describe how we calculate the effective constitutive relationships for the piezoelectric composites. To do so, we begin by stating the equations of motion of the piezoelectric medium, which are governed by the two following partial differential equations

$$\nabla \cdot \boldsymbol{\sigma} + \mathbf{f} = \dot{\mathbf{p}} \tag{1}$$

$$\nabla \cdot \mathbf{D} - q = 0 \tag{2}$$

where $\boldsymbol{\sigma}$ is the stress, $\mathbf{D}$ is the electric displacement, $\mathbf{p}$ is the momentum, $\mathbf{f}$ is the body force, and q is the prescribed free charge density. The stress $\boldsymbol{\sigma}$, electric displacement $\mathbf{D}$ and momentum $\mathbf{p}$ are related to the strain $\boldsymbol{\epsilon}$, gradient of electric potential $\nabla\phi$, inelastic strain $\boldsymbol{\eta}$ and velocity $\dot{\mathbf{u}}$ through the following constitutive relations as

$$\begin{bmatrix} \boldsymbol{\sigma} \\ \mathbf{D} \\ \mathbf{p} \end{bmatrix} = \begin{bmatrix} \mathbf{C} & \mathbf{B}^T & \mathbf{0} \\ \mathbf{B} & -\mathbf{A} & \mathbf{0} \\ \mathbf{0} & \mathbf{0} & \rho\mathbf{I} \end{bmatrix} \begin{bmatrix} \boldsymbol{\epsilon} - \boldsymbol{\eta} \\ \nabla\phi \\ \dot{\mathbf{u}} \end{bmatrix} \tag{3}$$

where $\mathbf{C}$ is the elastic tensor, and ρ is mass density, while $\mathbf{B}$ and $\mathbf{A}$ are piezoelectric and dielectric tensors, respectively.

By applying the ensemble averaging into the double governing Eqs. (1) and (2), the equations can be re-written as

$$\nabla \cdot \langle\boldsymbol{\sigma}\rangle + \mathbf{f} = \langle\dot{\mathbf{p}}\rangle \tag{4}$$

$$\nabla \cdot \langle\mathbf{D}\rangle - q = 0 \tag{5}$$

and the effective constitutive relations resulting from the homogenization approach, introduced by Shmuel et al. [23] are formed as

$$\begin{bmatrix} \langle\boldsymbol{\sigma}\rangle \\ \langle\mathbf{D}\rangle \\ \langle\mathbf{p}\rangle \end{bmatrix} = \begin{bmatrix} \bar{\mathbf{C}} & \bar{\mathbf{B}}^T & \bar{\mathbf{S}} \\ \bar{\mathbf{B}} & -\bar{\mathbf{A}} & \bar{\mathbf{W}} \\ \bar{\mathbf{S}}^\dagger & \bar{\mathbf{W}}^\dagger & \bar{\rho} \end{bmatrix} \begin{bmatrix} \langle\boldsymbol{\epsilon}\rangle - \boldsymbol{\eta} \\ \langle\nabla\phi\rangle \\ \langle\dot{\mathbf{u}}\rangle \end{bmatrix} \tag{6}$$

where $\langle\cdot\rangle$ denote ensemble averages, the overbars indicate effective tensors, and the † indicates adjoint operator with respect to

the spatial variable. The coupling terms $\bar{\mathbf{S}}$ and $\bar{\mathbf{W}}$ are responsible for the Willis coupling and the electro-momentum coupling, respectively. The structure for the coupled problem is illustrated by introducing symbolic notations as

$$\mathcal{L}=\begin{bmatrix}\mathbf{C} & \mathbf{B}^T & \mathbf{0}\\ \mathbf{B} & -\mathbf{A} & \mathbf{0}\\ \mathbf{0} & \mathbf{0} & \rho\mathbf{I}\end{bmatrix},\ \mathcal{D}^T=\begin{bmatrix}\nabla\cdot & 0 & -s\\ 0 & \nabla\cdot & 0\end{bmatrix},\ \mathcal{B}=\begin{bmatrix}\nabla & 0\\ 0 & \nabla\\ s & 0\end{bmatrix}$$
$$\mathbf{m}=\begin{bmatrix}\boldsymbol{\eta}\\ 0\\ 0\end{bmatrix},\ \mathbf{h}=\begin{bmatrix}\boldsymbol{\sigma}\\ \mathbf{D}\\ \mathbf{p}\end{bmatrix},\ \mathbf{g}=\begin{bmatrix}\mathbf{f}\\ -q\end{bmatrix},\ \text{and}\ \mathbf{w}=\begin{bmatrix}\mathbf{u}\\ \phi\end{bmatrix} \tag{7}$$

in which s represents the Laplace transform for the field variables with respect to derivative of time $\partial/\partial t$.

To enable the ensemble averaging approach that is applied with the dynamic homogenization of the piezoelectric medium, we follow the approach of Shmuel et al. [23] and define the Green's function and its boundary conditions as

$$\begin{cases}\mathcal{D}^T\mathcal{L}\mathcal{B}\mathbf{G}=-\begin{bmatrix}\mathbf{I}\delta\left(\mathbf{x}-\mathbf{x}'\right) & \mathbf{0}\\ \mathbf{0} & \delta\left(\mathbf{x}-\mathbf{x}'\right)\end{bmatrix}\\ \mathbf{G}\text{ is periodic on }\partial\Omega_w\\ (\mathcal{B}\mathbf{G})^T\mathcal{L}\mathbf{N}\text{ is anti-periodic on }\partial\Omega_t\end{cases} \tag{8}$$

with $\mathbf{N}^T=\begin{bmatrix}\otimes\mathbf{n} & 0 & 0\\ 0 & \otimes\mathbf{n} & 0\end{bmatrix}$.

Within use of the ensemble averaging, the effective operator $\bar{\mathcal{L}}$ is obtained in the following form

$$\bar{\mathcal{L}}=\langle\mathcal{L}\rangle-\left\langle\mathcal{L}\mathcal{B}(\mathcal{B}\mathbf{G})^T\mathcal{L}\right\rangle+\left\langle\mathcal{L}\mathcal{B}\mathbf{G}^T\right\rangle\langle\mathbf{G}\rangle^{-T}\left\langle(\mathcal{B}\mathbf{G})^T\mathcal{L}\right\rangle \tag{9}$$

Details of the derivation of Eq. (9) are shown in Ref. [23]. It is important that operators of $\bar{\mathcal{L}}$ corresponding to components in Eq. (6) are non-local operators in time and space. The constitutive operator $\bar{\mathcal{L}}$ provides finite terms $\bar{\mathcal{L}}_{23}$ and $\bar{\mathcal{L}}_{32}$ through the so-called electro-momentum couplings, denoted by $\bar{\mathbf{W}}$ which enable the average electric displacement $\langle\mathbf{D}\rangle$ to be coupled with $\langle\dot{\mathbf{u}}\rangle$ and the average momentum $\langle\mathbf{p}\rangle$ to be coupled with $\langle\nabla\phi\rangle$, respectively. If a multi-dimensional piezoelectric material model is examined, $\bar{\mathbf{W}}$ is a second-order tensor. It is analogous to properties of the original Willis couplings, mentioned in Refs. [4,32], the electro-momentum couplings generally appear in complex coefficients in which the imaginary part is due to asymmetric microstructures, and the real part is arising from non-local effects.

To numerically calculate the effective properties using the ensemble averaging, the Green's function defined in Eq. (8) is first numerically solved by deriving the Galerkin weak form over the unit cell domain Ω. Then by taking numerical integration to induce volume averages over terms in Eq. (9), the effective constitutive operator in Eq. (6) is numerically obtained. Appendix A shows details of the numerical algorithm in which the effective constitutive relations of periodic piezoelectric media are extended to Bloch wave solutions.

3. Numerical examples

In this section, several examples are solved to elucidate the nature of the electro-momentum coupling, and to verify the ensemble averaging approach for the dynamic homogenization of composite piezoelectric materials. Specifically, a 1D problem is analyzed and compared with the analytical solution proposed by Salomón and Shmuel [23]. Next, a 2D numerical homogenization model based on the ensemble average is established for a unit cell made from two different piezoelectric phases. A genetic optimization algorithm is then designed to seek the optimal material distributions such that the electro-momentum coupling is maximized. Finally, the obtained unit cells are used to examine how the electro-momentum coupling impacts wave propagation in a piezoelectric metamaterial.

Table 1
Material parameters.

Material	C (GPa)	ρ (kg/m^3)	B (C/m^2)	A (nF/m)
PZT4	115	7500	15.1	5.6
$BaTiO_3$	165	6020	3.64	0.97
PVDF	12	1780	−0.027	0.067
SiO_2	74	2160	0.066	0.02
Al_2O_3	300	3720	0	0.079
PMMA	3.3	1188	0	0.023

3.1. 1D validation

We first verify the ensemble averaging approach for a 1D case. Specifically, we analyze the problem proposed by Shmuel et al. [23], in which three unit cells with length $l = 3$ mm are composed of different 3-layered piezoelectric materials. Their compositions are made from and are ordered in a $l_a l_b l_c$ ordering as: PZT4-$BaTiO_3$-PVDF (composition 1), Al_2O_3-PZT4-PMMA (composition 2), and PZT4-$BaTiO_3$-SiO_2 (composition 3). The length distribution of microstructures is arranged in order $l_a = 1$ mm, $l_b = 1.4$ mm and $l_c = 0.6$ mm. The material parameters of these layers are provided in Table 1. Deformation of the composite is induced by a body force, where the electric displacement D and surface charge are set to be zero. Accordingly, the analytic solution based on a single Green's function is constructed to calculate the effective properties. For the present numerical analysis, the idea of using single Green's function is still employed in the ensemble average framework. Due to the periodicity of the structure, Bloch waves are admitted to produce numerical solutions specified by the wave vector k and the frequency ω.

Fig. 2 shows the evolution of the electro-momentum coupling computed for $kl = 2$ at low frequencies for composition 1 (PZT4-$BaTiO_3$-PVDF). We note that the symmetric case given in Fig. 2(b) is created with $l_b = 0$, $l_a = l_c = 1.5$ mm. As shown in Fig. 2, the electro-momentum couplings are activated when $\omega > 0$. Furthermore, the imaginary parts of $\bar{W}$ and $\bar{W}^\dagger$ are equal while the real parts are opposite to each other. In other words, the relations satisfy the symmetric property $\bar{W}(k,\omega) = -\text{conj}\left(\bar{W}^\dagger(k,\omega)\right)$ presented in Refs. [23,24], which is equivalent to the expression of their Fourier transform. This feature is identical to that of the original elasto-momentum couplings $\bar{S}(k,\omega) = -\text{conj}\left(\bar{S}^\dagger(k,\omega)\right)$mentioned in Refs. [4,7,11,13]. It should be noted in Fig. 2(b) that Imag $\left(\bar{W}\right)$ and Imag $\left(\bar{W}^\dagger\right)$ vanish under the symmetry of the unit cell, due to the requirement that the imaginary parts of the electro-momentum coupling arise from geometric asymmetry. These results match well with the analytic results shown in Ref. [23].

Fig. 3 illustrates the evolution of the electro-momentum coupling $\bar{W}$ against the frequency ω for the situation where waves with wavelength $kl = 0$ and $kl = 2$ are imposed on piezoelectric cells with composition 2 (Al_2O_3-PZT4-PMMA). As for the magnitude of Imag $\left(\bar{W}\right)$, composition 1 generates maximal values with only about 20 and 7 μCs/m^3 as shown in Fig. 2. While composition 2 with lower absolute values of the ratio between the piezoelectric coefficient and the permittivity generates significantly higher electro-momentum values of over 900 and 1400 μCs/m^3 corresponding to the case $kl = 0$ and $kl = 2$, respectively. Interestingly, this demonstrates that while the ratios of $|B/A|$ over materials comprising composition 2 are significantly lower than those comprising composition 1, the electro-momentum coupling values of composition 2 is significantly higher than that of composition 1.

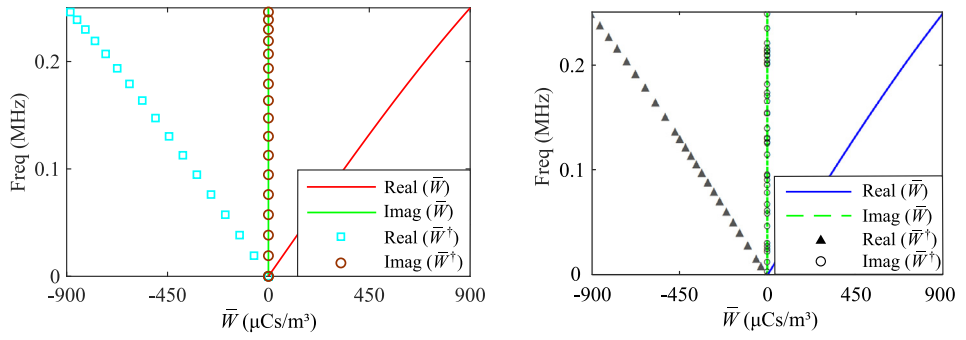

(a) Symmetric 1D structure: numerical results (b) Symmetric 1D structure: Salomón's results

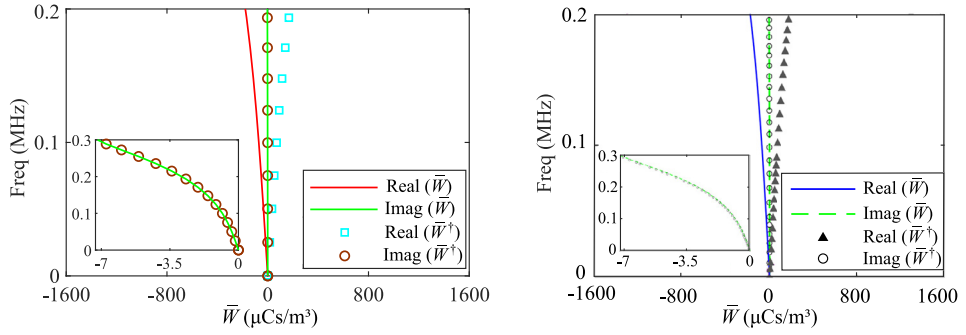

(c) Asymmetric 1D structure: numerical results (d) Asymmetric 1D structure: Salomón's results

Fig. 2. Electro-momentum coupling of composition 1 at $kl = 2$, obtained from the numerical approach, and the analytical solution derived by Shmuel et al. [23].

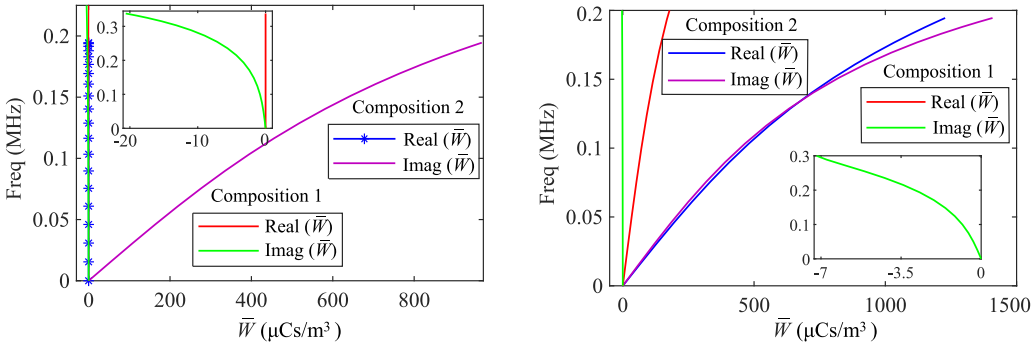

(a) $kl = 0$ (b) $kl = 2$

Fig. 3. Electro-momentum coupling of composition 2, compared with that of composition 1.

A further examination of electro-momentum coupling $\bar{W}$ at $kl = 0$, and $\omega = 0.1$ MHz on the three compositions is carried out by setting $l_a = l_c$ and $0 \leq l_b \leq l$. As shown in Fig. 4, Imag $(\bar{W})$ would vanish at $l_b = 0$ mm and $l_b = 3$ mm correspondingly where the unit cells are symmetric, and their materials are uniform. Looking at the diagram of composition 1, there is a singularity around $l_b = 0.87$ mm, which arises from it being comprised of piezoelectric materials with coefficients of different sign. Furthermore, the electro-momentum from composition 2 shows a jump discontinuity at the right limit $l_b \to 0^+$, which corresponds to the point when all materials in the unit cell are elastic, but not piezoelectric. These results agree well with data from the analytical solution shown in Ref. [23]. As for the appearance of composition 3, it shows much lower values than the two first compositions, although its material components are different from composition 1 in only SiO_2 instead of PVDF. It appears that the combination of materials with opposite polarization coefficients like composition 1 can result in a singularity in the electro-momentum coupling.

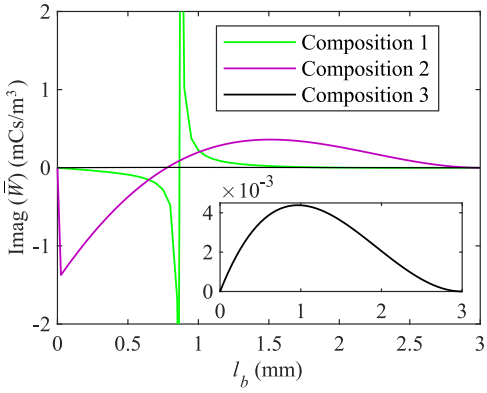

Fig. 4. Imag $(\bar{W})$ with variation of l_b while $l_a = l_c$.

Moreover, if the analogous examination is executed with $kl \neq 0$, the trends of the electro-momentum for three compositions here are similar to the case $kl = 0$. In particular, there are still special points from composition 1 and composition 2. By considering at $kl = 2$, $\omega = 0.1$ MHz, the singular point of composition 1 is at $l_b = 0.9$ mm, while the vanishing point moves to 0.75 mm for composition 2.

3.2. Maximizing the electro-momentum coupling in 2D

Having verified the effective constitutive relations in 1D, we now progress to developing a computational technique to design a 2D microstructure comprising piezoelectric materials to maximize the electro-momentum coupling $\bar{\mathbf{W}}^{\dagger}$. Such computational approaches are required because while layered structures are the only possibility for composites in 1D, the design space for 2D composites is significantly larger.

3.2.1. Topology optimization method to maximize the electro-momentum coupling

To formulate the design problem, we begin with the constitutive relations shown in Eq. (6), then re-write the macroscopic momentum as compositions of the momentum due to strain $\langle \mathbf{p}^{\varepsilon} \rangle$, electric field $\langle \mathbf{p}^{e} \rangle$ and velocity $\langle \mathbf{p}^{v} \rangle$, in which the term $\langle \mathbf{p}^{e} \rangle$ is expressed as

$$\left\langle \tilde{\mathbf{p}}^{e} \right\rangle = \bar{\mathbf{W}}^{\dagger} \left(\nabla + i\mathbf{k}\right) \left\langle \tilde{\phi} \right\rangle \tag{10}$$

By applying the divergence theorem for $\tilde{\phi}$, we have $\int_{\Omega} \nabla \tilde{\phi} d\Omega = \int_{\partial\Omega} \tilde{\phi} \mathbf{n} da = \mathbf{0}$. Consequently, Eq. (10) can be written in terms of its components as

$$\begin{bmatrix} \left\langle \tilde{p}^{e} \right\rangle_x \\ \left\langle \tilde{p}^{e} \right\rangle_y \end{bmatrix} = \begin{bmatrix} \bar{W}^{\dagger}_{xx} & \bar{W}^{\dagger}_{xy} \\ \bar{W}^{\dagger}_{yx} & \bar{W}^{\dagger}_{yy} \end{bmatrix} \begin{bmatrix} ik_x \\ ik_y \end{bmatrix} \left\langle \tilde{\phi} \right\rangle \tag{11}$$

In proceeding to optimize a unit cell to maximize $\bar{\mathbf{W}}^{\dagger}$, we work at longer wavelengths/lower frequencies over the acoustic band. The unit cells are assumed to satisfy Bloch periodicity, where the mechanical and electrical fields can be written in terms of the wavenumber $\mathbf{k}$ and the frequency ω, such that the effective tensor $\bar{\mathbf{W}}^{\dagger}$ is consequently related to $(\mathbf{k}, \omega)$. For simplicity, we assume that we wish to maximize the electro-momentum coupling only in the y-direction, which implies that $\bar{W}^{\dagger}_{yx}$ and $\bar{W}^{\dagger}_{yy}$ are the components of $\bar{\mathbf{W}}^{\dagger}$ that should be maximized. The equivalent electro-momentum in the y-direction is as follows,

$$\bar{W}^{\dagger}_{y} = \frac{\left(\bar{W}^{\dagger}_{yx} k_x + \bar{W}^{\dagger}_{yy} k_y\right)}{\|\mathbf{k}\|} \tag{12}$$

We aim to maximize the imaginary portion of $W^{\dagger}_{y}$ that is needed to generate wave propagation asymmetry resulting from the electro-momentum coupling. To do so, the discretization model is employed to compute the overall constitutive properties and the parameters for optimization as well. The design domain Ω is first discretized into sub-domains Ω_D. The objective function is defined as a minimization problem via inversion of $\bar{W}^{\dagger}_{y}$ at the frequency ω and wavenumber $\mathbf{k}$

$$\text{Minimize } J(\boldsymbol{\alpha}) = \frac{1}{\left|\text{Imag}\left(\bar{W}^{\dagger}_{y}\right)\right|} \tag{13a}$$

$$\text{Subject to: } \alpha_e(\mathbf{x}) \in [0, 1], \; e \in \Omega_D$$

$$\boldsymbol{\alpha}\left(\mathbf{x} \in \partial\Omega^{l}\right) = \boldsymbol{\alpha}\left(\mathbf{x} \in \partial\Omega^{r}\right), \text{ and} \tag{13b}$$

$$\boldsymbol{\alpha}\left(\mathbf{x} \in \partial\Omega^{b}\right) = \boldsymbol{\alpha}\left(\mathbf{x} \in \partial\Omega^{t}\right)$$

where Eq. (13b) shows constraints of the optimization problem. In detail, values 0 and 1 in the first line are represented for two-phase piezoelectric materials, and thus each phase will be identified in a corresponding value of the elemental design variable α_e. The second line presents the constraint of periodic material distributions on opposite edges of the unit cell whose the boundaries are labeled in Fig. 5.

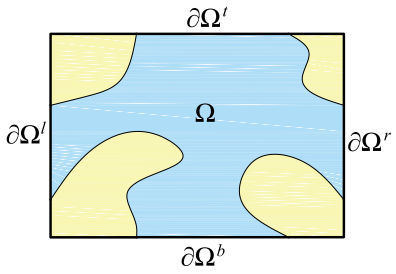

Fig. 5. Schematic of periodic 2D material with boundaries labeled for the design domain.

Table 2
Material properties of PZT4.

C (GPa)			**B** (C/m^2)			**A** (nF/m)		ρ (kg/m^3)
139	74.3	0	0	0	12.7	5.6	0	7500
74.3	115	0	−5.2	15.1	0	0	5.6	
0	0	25.6						

Table 3
Material properties of PVDF.

C (GPa)			**B** (C/m^2)			**A** (nF/m)		ρ (kg/m^3)
6.5	4.3	0	0	0	0	0.067	0	1780
4.3	6.5	0	0.023	−0.033	0	0	0.067	
0	0	1.08						

The design sensitivity of the objective function is solved using a genetic algorithm (GA), which has previously been applied in topology optimization problems [33–35], where further details on the fundamentals of GAs can be found in Refs. [33,36]. The GA population is in terms of a set of binary strings. The binary digits in a string are mapped into the FE meshes where elements are assigned with values of 1 responsible for the distributions of material 1 while those with allele values of 0 correspond to material 2, as shown in Fig. 6. Particularly, we use a structure with only 8×8 pixels to clearly illustrate steps of decoding a binary string representation into a meaningful topology in a design domain. In the examples, the number of pixels used in the analysis is 40×40 that is observed to be sufficient to generate a stable optimal topology. Following the present topology optimization, the level set method [37] is used to smoothly track interfaces between material phases. Details about the finite element formulation evolving the optimization computations are provided in Appendix A.

We set up calculations on a square unit cell with the size $a = 5$ mm that is made of PZT4 and PVDF, where the corresponding material properties are given in Tables 2 and 3. Bloch waves are propagated in the plane with the form $\mathbf{w} = \tilde{\mathbf{w}} e^{i(k_0 \cos\theta + k_0 \sin\theta - \omega t)}$ where the angle θ which is defined counter-clockwise with respect to x-direction is chosen to be 75^0, and the wavenumber is managed as $k_0 = 0.5/a$, while the frequency was specified to be 50 kHz.

The GA-based optimization for the present work is run with a randomly generated initial population of 500 individuals constrained by identical material distributions on each pair of opposite edges. The solution to the optimization problem converges

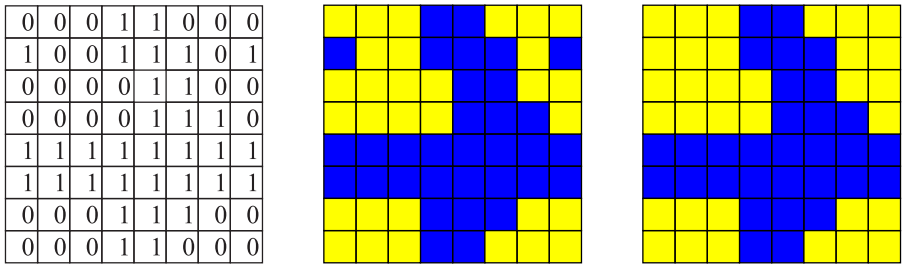

Fig. 6. Formation of a design domain: (a) Rearranged binary string with the binary digits assigned to the finite elements, (b) resulting topology where material 1 (in blue) corresponds to values of 1 and material 2 (in yellow) corresponds to values of 0, (c) refined topology that small disconnected components are removed. (For interpretation of the references to color in this figure legend, the reader is referred to the web version of this article.)

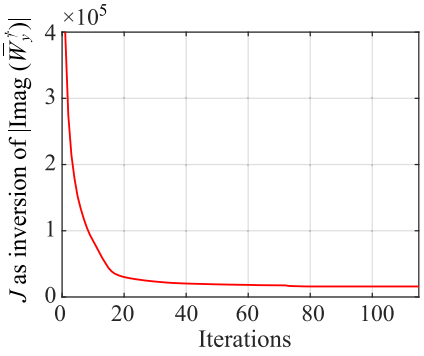

Fig. 7. Convergence rate of the objective function J.

at the rate shown in Fig. 7: the objective function falls below the tolerance value after over 100 function evaluations of the defined electro-momentum FE formulation (see Fig. 8).

The unit cell that results from the optimization process to maximize $\bar{W}_y^{\dagger}$ in Eq. (12) is shown in Fig. 8(a). We first observe that the optimized microstructure is asymmetric, which is consistent with the notion that the presence of the imaginary part of the electro-momentum coupling arises from broken inversion symmetry, as discussed in Ref. [23]. This feature is analogous to the conventional Willis coupling arising from the asymmetry in elasticity [14,32]. Fig. 8(b) shows the imaginary values of components in $\bar{\mathbf{W}}^{\dagger}$ in the range from 0 to 60 kHz. As expected, the contribution of the imaginary parts of the y-directional components, i.e. of $\bar{W}_{yx}^{\dagger}$ and $\bar{W}_{yy}^{\dagger}$ to $\langle\tilde{p}^e\rangle_y$, is much larger than the imaginary parts of the electro-momentum coupling tensors related to the x-direction $\langle\tilde{p}^e\rangle_x$. This demonstrates the optimized unit cell in Fig. 8(a) demonstrates a strong electro-momentum coupling in the y-direction, as expected from the optimization.

3.2.2. Modeling wave propagation

To determine the effect of the electro-momentum coupling on wave propagation, we design a 2D metamaterial structure made of optimized unit cells placed side by side into the middle of a PVDF beam along the y-direction as shown in Fig. 9, where the structure containing 5 optimized unit cells serves as the reference structure of interest to examine the emergence of generalized Willis phenomena. We generate motion by applying displacements with the amplitude $|u_0| = 2e^{-4}$ m at $y = 0$. For the case of forward waves, the source is placed at the left-hand side of the beam ($y = 0$) along x-direction and the forward displacement amplitude u_y^f is observed at a point located at $1e^{-2}$ m behind the last optimized unit cell while the backward waves are conducted in the same manner, where the same displacement amplitude is applied at $y = L$, while the backward displacement amplitude u_y^b is observed at a point located at $1e^{-2}$ m behind the first optimized unit cell. The amplitudes of forward and backward waves are normalized by a factor $1.5u_y^{max}$, and correspond to t^f and t^b. The percent difference between t^f and t^b, defined by $\Delta t = \left||t^f| - |t^b|\right|$ is used to measure the asymmetric level of waves. We obtain these wave amplitudes by solving the coupled field in Eqs. (4) and (5), where details on the finite element discretization for numerically solving these equations are included in Appendix B. The simulations are examined within the 2D real space, over the frequency domain from 50 to 60 kHz, and the

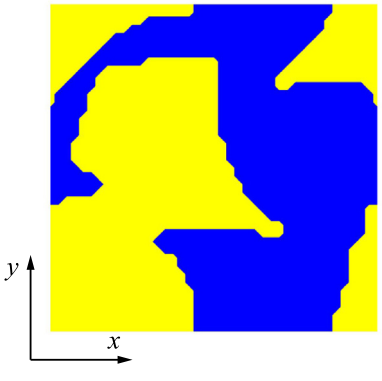

(a)

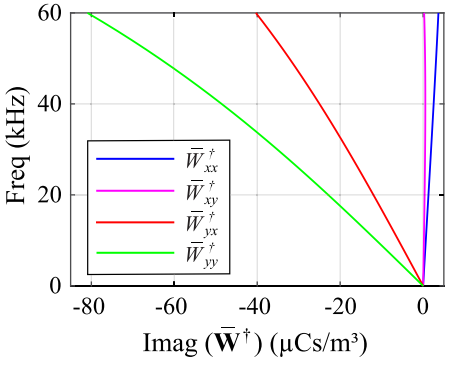

(b)

Fig. 8. (a) Optimized bi-material unit cell, (b) Imaginary part of components in $\bar{W}^{\dagger}$.

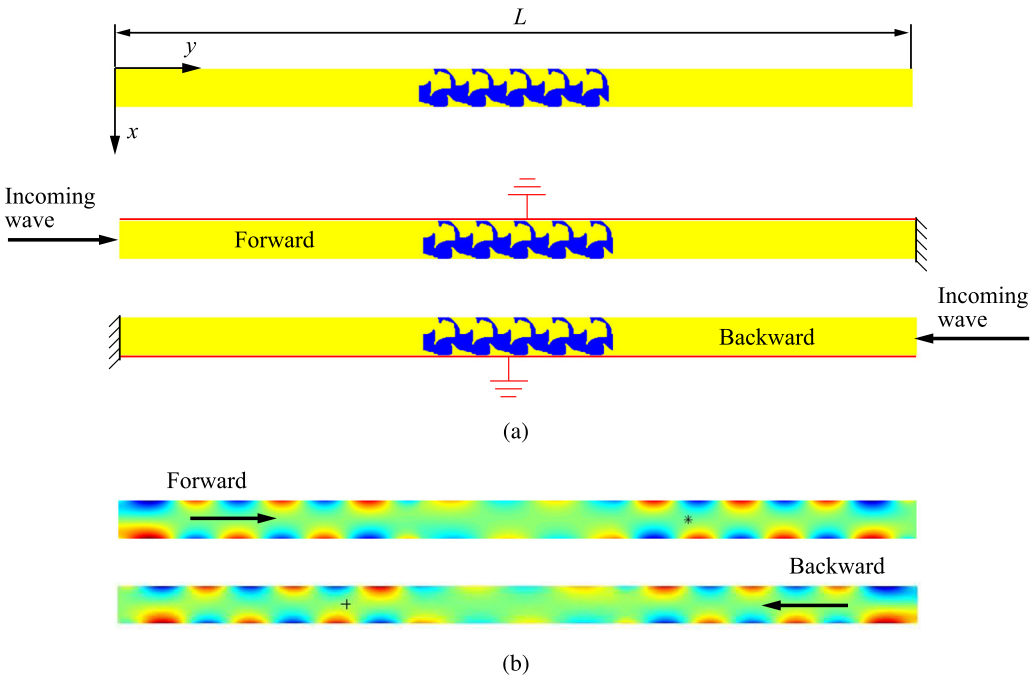

Fig. 9. Schematic of the metamaterial system: (a) supercell and boundary conditions imposed to generate forward/backward wave, and (b) displacement field u_y of forward/backward waves in order to study the effect of electro-momentum coupling on asymmetric wave propagation. At a frequency of 53 kHz, the normalized amplitude of displacement in y-direction of the forward wave, $|t^f|$ at observation point marked in black star is 0.36, while the normalized amplitude of displacement in y-direction of the backward wave, $|t^b|$ at the point marked in black plus is 0.45.

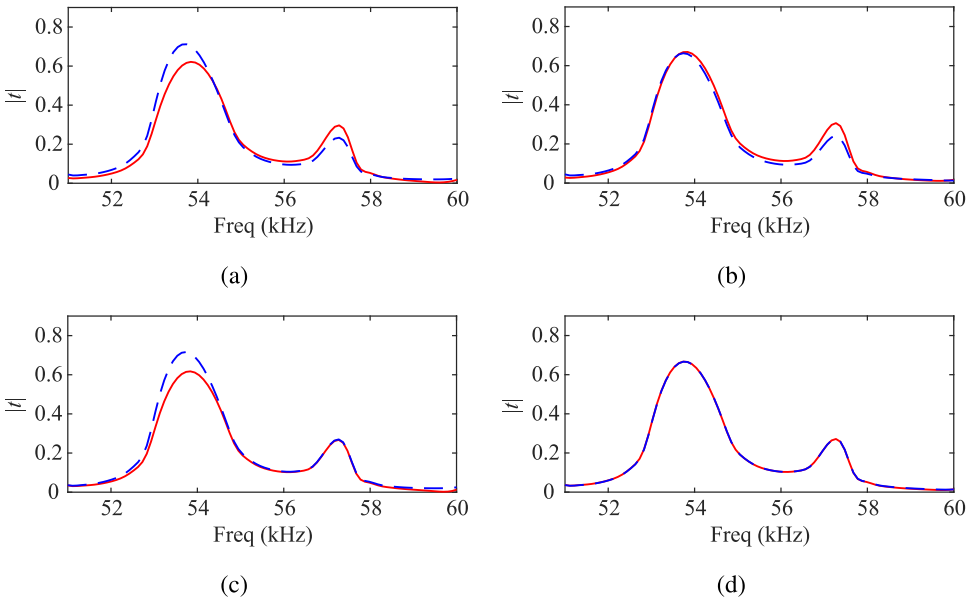

Fig. 10. Amplitudes of waves where the constitutive relations of piezoelectric Willis materials that: (a) Account for both elasto-momentum ($\bar{\mathbf{S}}$) and electro-momentum ($\bar{\mathbf{W}}$) coupling; (b) Neglect elasto-momentum coupling ($\bar{\mathbf{S}}$); (c) Neglect electro-momentum coupling ($\bar{\mathbf{W}}$), and (d) Neglect both elasto-momentum ($\bar{\mathbf{S}}$) and electro-momentum ($\bar{\mathbf{W}}$) coupling. The red and blue lines correspond to forward and backward waves. (For interpretation of the references to color in this figure legend, the reader is referred to the web version of this article.)

wavenumber specified at $k_0 = 0.5/a$ and $\theta = 75°$. The metamaterial beam is fixed on the right-hand side, while the voltage is prescribed to be grounded on the top of the beam for the case of forward waves. Similarly, the beam displacements on the left-hand side are fixed while the voltage is grounded on the bottom of the beam for the case of backward waves.

The amplitudes for forward and backward propagating waves are plotted in Fig. 10, where we considered four different cases for the effective constitutive relationships. In all cases, the amplitudes of the waves are maximized at about 53.8 and 57.2 kHz. Fig. 10(a) shows the amplitude of both forward and backward waves when both electro-momentum ($\bar{\mathbf{W}}$) and elasto-momentum ($\bar{\mathbf{S}}$) couplings are accounted for, where there are clear differences, and thus asymmetry, in the amplitudes $|t|$ of waves propagated in forward and backward directions. To delineate the effect of electro-momentum as compared to elasto-momentum coupling

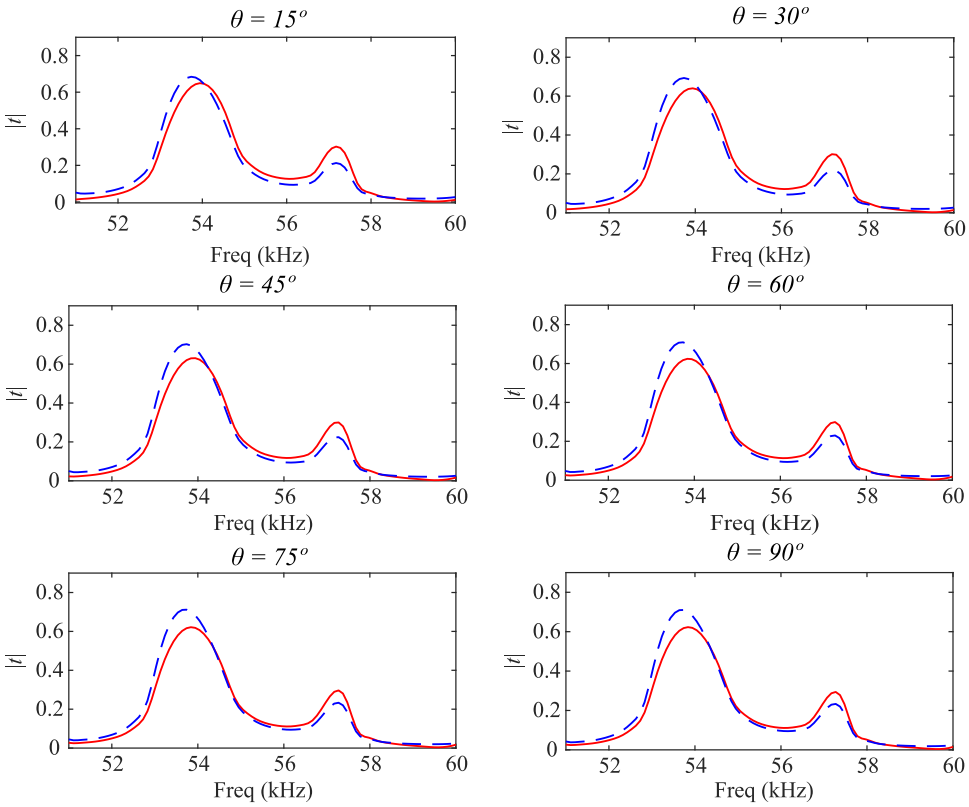

Fig. 11. Amplitudes of waves with the variation of wavenumber obtained with various angles θ. The red and blue lines correspond to forward and backward waves. (For interpretation of the references to color in this figure legend, the reader is referred to the web version of this article.)

in enabling the asymmetry, we considered cases where either elasto-momentum (Fig. 10(b)) or electro-momentum (Fig. 10(c)) coupling were neglected. By neglecting elasto-momentum, we see in Fig. 10(b) that the asymmetry is largest at a frequency of 57.2 kHz, with an asymmetric percentage $\Delta t = 6.7$. In contrast, when electro-momentum is neglected as in Fig. 10(c), the asymmetry is largest at a frequency of about 53.8 kHz, with an asymmetric percentage $\Delta t = 9.8$. Thus, while the wave amplitude is larger at 53.8 kHz, the electro-momentum coupling generates a proportionally larger asymmetric response at 57.2 kHz. Finally, if both electro and elasto-momentum coupling are neglected, there is no asymmetry in the wave propagation, as shown in Fig. 10(d).

While the results in Fig. 10 were for a specific $\theta = 75°$, we now examine the effects of varying θ, which is a proxy for changing the wavenumber. The wave amplitudes shown in Fig. 11 have the same trend at different values of θ, and are locally maximal at the same two frequencies, i.e. 53.8 and 57.2 kHz. Table 4 shows the difference of the asymmetric amplitudes Δt, observed at the two prominent points, along with the frequency of 50 kHz used for the optimization. At the first key frequency 53.8 kHz, the largest asymmetry Δt is achieved at $\theta = 75°$, which coincides with the given chosen value for the optimization computation, while the asymmetry for the second peak is maximized at $\theta = 15°$.

We next determine the effect of the number of asymmetric unit cells in the piezoelectric metamaterial beam on the asymmetry. Thus, we conducted simulations with $\theta = 75°$ on the metamaterial beam using either 3 or 5 optimized unit cells to examine that effect on the asymmetric wave propagation. Fig. 12 shows amplitudes obtained from the metamaterial beam with 3 and 5 optimized unit cells. The asymmetric amplitudes from the 3-cell specimen are also prominent at two frequencies, though their values are different are shifted slightly to 53 and 56 kHz, respectively, leading to difference of amplitudes Δt of 6 and 12 percent at those frequencies. This is in contrast to the 5-cell specimen, which had maximum percentage difference in amplitudes Δt of 9 and 6.4 at 53.8 and 57.2 kHz. It is clear that the asymmetric behavior is observed for different numbers of optimized unit cells, though the specific frequencies at which it is maximized may clearly shift as a result.

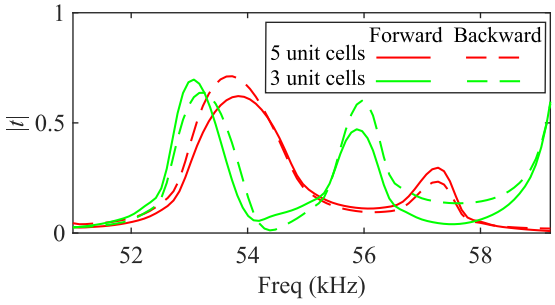

Fig. 12. Amplitudes of waves over the beam with 3 optimized unit cells.

Table 4
Asymmetric wave propagation, as measured by percent difference in forward and backward wave amplitudes $\Delta t = \left||t^f| - |t^b|\right|$ with respect to angle θ.

Freq	θ					
	15°	30°	45°	60°	75°	90°
50	0.3	0.3	0.3	0.4	0.4	0.4
53.8	3.5	6.3	7.3	8.5	9	8.7
57.2	8.7	8.1	7.5	6.9	6.4	6.1

Finally, we examine the nature of the asymmetric wave propagation when the stimulus to induce wave propagation is electrical in nature, and not mechanical. To do so, we excited the long side of the 5-cell beam using an electric potential $\phi_0 = 5e^5$ V to drive

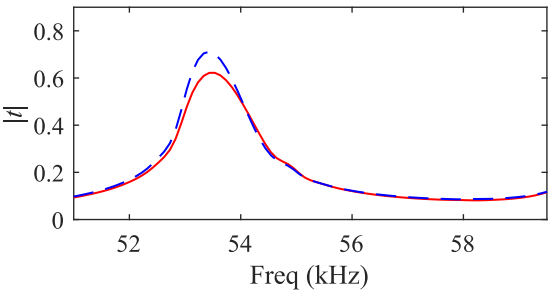

Fig. 13. Amplitudes of waves excited by the electrical source. The red and blue lines correspond to forward and backward waves. (For interpretation of the references to color in this figure legend, the reader is referred to the web version of this article.)

wave propagation. Fig. 13 shows the asymmetric wave amplitudes for both directions obtained at $\theta = 75°$. In comparison with the case of using mechanical excitation shown Fig. 10(a), the present investigation has only one prominent point at nearly 53.5 kHz. The use of the electrical excitation also produces asymmetric waves with percent difference in amplitude of $\Delta t = 9$ at 53.5 kHz. It is interesting that when electrical loading is utilized, we observe only one frequency maximum, rather than two as seen in mechanical loading. This is expected, as the electro-momentum couplings in Eq. (6) through the complex conjugates are not symmetric, and as such a different response may be expected depending on the physical nature (mechanical vs. electrical) of the loading.

4. Conclusion

In this work, we have developed a numerical framework to enable, through dynamic homogenization, the design of piezoelectric composites which demonstrate a novel form of Willis coupling, the so-called electro-momentum coupling [23], in which the macroscopic momentum is additionally coupled with the electric fields. In particular, we have developed a topology optimization approach to maximize the electro-momentum coupling, and demonstrated that the obtained unit cells can be used to drive asymmetric wave propagation in a 2D piezoelectric metamaterial that is excited by either mechanical or electrical stimuli. Our examples demonstrated that the asymmetric wave propagation is driven by a combination of traditional elasto-momentum coupling, as well as the new electro-momentum coupling, which opens the door to designing novel materials that enable asymmetric wave phenomena through electro-mechanical coupling effects.

Declaration of competing interest

The authors declare that they have no known competing financial interests or personal relationships that could have appeared to influence the work reported in this paper.

Data availability

Data will be made available on request.

Acknowledgments

The authors gratefully acknowledge the sponsorship from NSFC, China (52278411) and the Science and Technology Commission of Shanghai Municipality, China (22JC1404100). Authors also acknowledge the support of the HLRN project and cluster system team at the Leibniz Universität of Hannover, Germany.

Appendix A. Numerical computation of the effective properties

To numerically perform the dynamic homogenization, the unit cell domain is first discretized into 4-node quadrilateral finite elements, which will contain information for the material distributions, which is important for the subsequent topology optimization.

Since the field variables $\mathbf{w} = \begin{bmatrix} \mathbf{u} \\ \phi \end{bmatrix}$ are specialized to Bloch waves assuming unit cell periodicity Ω, they are formed as $\mathbf{w}(\mathbf{x}) = \tilde{\mathbf{w}}(\mathbf{x}) e^{i(\mathbf{k}\cdot\mathbf{x}-\omega t)}$. Similarly, the Green's function, as a solution of Eq. (8) is also extended to the Bloch form. We develop the numerical formulation by applying the weak form on Eq. (8) in terms of $\tilde{\mathbf{G}}^\dagger$. In detail, by multiplying by the test function $\delta\tilde{\mathbf{G}}^T$, taking integration over Ω, and applying Green's theorem, we obtain the numerical solution of the Green's function as

$$\begin{aligned} &\int_\Omega \left(\delta\tilde{\mathbf{G}}^T\right)(\mathcal{B}+i\mathbf{k})^T \mathcal{L}\,(\mathcal{B}-i\mathbf{k})\,\tilde{\mathbf{G}}^\dagger\left(\mathbf{x}-\mathbf{x}'\right)d\Omega \\ &= \int_\Omega \left(\delta\tilde{\mathbf{G}}^T\right)\begin{bmatrix} \mathbf{I}\delta\left(\mathbf{x}-\mathbf{x}'\right) & \mathbf{0} \\ \mathbf{0} & \delta\left(\mathbf{x}-\mathbf{x}'\right) \end{bmatrix} d\Omega \end{aligned} \tag{A.1}$$

The notation $\tilde{\mathbf{G}}^\dagger(\mathbf{x}-\mathbf{x}')$ is simplified by $\tilde{\mathbf{G}}^\dagger$, in which the term on the left of $\tilde{\mathbf{G}}^\dagger$ depends on vector position $\mathbf{x}$, and the term on the right depends on $\mathbf{x}'$. The development of Eq. (A.1) leading to the matrix form of the finite element approach is given by

$$\mathcal{K}\tilde{\mathbf{G}}^\dagger = \mathbf{I} \tag{A.2}$$

Within the finite element discretization, the local matrix $\mathcal{K}^e$ (the superscript "e" corresponds to the eth element) is defined as

$$\mathcal{K}^e = \int_{\Omega^e} (\mathcal{B}+i\mathbf{k})^T \mathcal{L}\,(\mathcal{B}-i\mathbf{k})\,d\Omega \tag{A.3}$$

in which

$$\mathcal{B}^i = \begin{bmatrix} \frac{\partial\mathcal{N}^i}{\partial x} & 0 & \frac{\partial\mathcal{N}^i}{\partial y} & 0 & 0 & s\mathcal{N}^i & 0 \\ 0 & \frac{\partial\mathcal{N}^i}{\partial y} & \frac{\partial\mathcal{N}^i}{\partial x} & 0 & 0 & 0 & s\mathcal{N}^i \\ 0 & 0 & 0 & \frac{\partial\mathcal{N}^i}{\partial x} & \frac{\partial\mathcal{N}^i}{\partial y} & 0 & 0 \end{bmatrix}^T,$$

$$\mathcal{B} = \begin{bmatrix} \mathcal{B}^1 & \mathcal{B}^2 & \dots & \mathcal{B}^n \end{bmatrix}$$

where n is the number of nodes of the current element, and $\mathcal{N}^i$ is the basis function of the node ith. Next, we follow the definition to take the mean value of a periodic function $\tilde{\mathbf{h}}$ within the ensemble averaging, presented in Ref. [4] as

$$\left\langle\tilde{\mathbf{h}}\right\rangle(\mathbf{x}) = \frac{1}{|\Omega|}\int_\Omega \tilde{\mathbf{h}}\left(\mathbf{x},\mathbf{x}'\right)d\mathbf{x}' \equiv \left\langle\tilde{\mathbf{h}}\right\rangle_{\mathbf{x}'} \tag{A.4}$$

Note that notation $\langle\bullet\rangle_{\mathbf{x}'}$ is represented for the average-over-Ω operator in the vector position $\mathbf{x}'$. The above equation is applied into relation $\mathbf{h}(\mathbf{x}) = \mathcal{L}(\mathcal{B}\mathbf{w}-\mathbf{m})(\mathbf{x})$, and its mean value is obtained by

$$\langle\mathbf{h}\rangle = \bar{\mathcal{L}}\left(\langle\mathcal{B}\mathbf{w}\rangle - \mathbf{m}\right) \tag{A.5}$$

From the resultant ensemble averaging definitions of Eq. (A.5), the overall constitutive operator in Eq. (9) is finally obtained by

$$\begin{aligned} \bar{\mathcal{L}} = \langle\mathcal{L}\rangle_{\mathbf{x}} &- \left\langle\left\langle\mathcal{L}\,(\mathcal{B}+i\mathbf{k})\left((\mathcal{B}-i\mathbf{k})\,\tilde{\mathbf{G}}^\dagger\right)^T\mathcal{L}\right\rangle_{\mathbf{x}'}\right\rangle_{\mathbf{x}} \\ &+ \left\langle\left\langle\mathcal{L}\,(\mathcal{B}+i\mathbf{k})\left(\tilde{\mathbf{G}}^\dagger\right)^T\right\rangle_{\mathbf{x}'}\right\rangle_{\mathbf{x}}\left\langle\left\langle\tilde{\mathbf{G}}^\dagger\right\rangle_{\mathbf{x}'}\right\rangle_{\mathbf{x}}^{-T}\left\langle\left\langle\left((\mathcal{B}-i\mathbf{k})\,\tilde{\mathbf{G}}^\dagger\right)^T\mathcal{L}\right\rangle_{\mathbf{x}'}\right\rangle_{\mathbf{x}} \end{aligned} \tag{A.6}$$

Appendix B. Numerical computation of the macroscopic effects

From the obtained effective properties in Eq. (6), these relations are taken into the governing Eqs. (4), (5) to model electromechanical effects on the structures. With the domain of the structure, sub-divided into quadrilateral finite elements, the Galerkin method is employed in solving Eq. (4) and (5). The numerical solution for the field variables $\begin{bmatrix} \langle \mathbf{u} \rangle \\ \langle \phi \rangle \end{bmatrix}$ in terms of the periodicity is defined as

$$\begin{bmatrix} \mathbf{K}_{uu} - \omega^2 \mathbf{M} & \mathbf{K}_{u\phi} \\ \mathbf{K}_{\phi u} & \mathbf{K}_{\phi\phi} \end{bmatrix} \begin{bmatrix} \langle \tilde{\mathbf{u}} \rangle \\ \langle \tilde{\phi} \rangle \end{bmatrix} = \begin{bmatrix} \mathbf{r}_u \\ \mathbf{r}_\phi \end{bmatrix} \tag{B.1}$$

The local contributions of components in Eq. (B.1) corresponding to element eth are given by

$$\mathbf{K}^e_{uu} = \int_{\Omega^e} \left[(\mathcal{B}_u - i\mathbf{k})^T \bar{\mathbf{C}} (\mathcal{B}_u + i\mathbf{k}) + s(\mathcal{B}_u - i\mathbf{k})^T \bar{\mathbf{S}} \mathcal{N}_u + s\mathcal{N}_u^T \bar{\mathbf{S}}^\dagger (\mathcal{B}_u + i\mathbf{k}) \right] d\Omega \tag{B.2a}$$

$$\mathbf{K}^e_{u\phi} = \int_{\Omega^e} \left[(\mathcal{B}_u - i\mathbf{k})^T \bar{\mathbf{B}}^\dagger \left(\mathcal{B}_\phi + i\mathbf{k}\right) + s\mathcal{N}_u^T \bar{\mathbf{W}}^\dagger \left(\mathcal{B}_\phi + i\mathbf{k}\right) \right] d\Omega \tag{B.2b}$$

$$\mathbf{K}^e_{\phi u} = \int_{\Omega^e} \left[\left(\mathcal{B}_\phi - i\mathbf{k}\right)^T \bar{\mathbf{B}} (\mathcal{B}_u + i\mathbf{k}) + s\left(\mathcal{B}_\phi - i\mathbf{k}\right)^T \bar{\mathbf{W}} \mathcal{N}_u \right] d\Omega \tag{B.2c}$$

$$\mathbf{K}^e_{\phi\phi} = -\int_{\Omega^e} \left(\mathcal{B}_\phi - i\mathbf{k}\right)^T \bar{\mathbf{A}} \left(\mathcal{B}_\phi + i\mathbf{k}\right) d\Omega \tag{B.2d}$$

$$\mathbf{M}^e = \int_{\Omega^e} \mathcal{N}_u^T \bar{\boldsymbol{\rho}} \mathcal{N}_u d\Omega \tag{B.2e}$$

$$\mathbf{r}^e_u = \int_{\Omega^e} \mathcal{N}_u^T \mathbf{f} d\Omega + \int_{\partial\Omega^e_t} \mathcal{N}_u^T \mathbf{t} da \tag{B.2f}$$

$$\mathbf{r}^e_\phi = -\int_{\Omega^e} \mathcal{N}_\phi^T q d\Omega - \int_{\partial\Omega^e_w} \mathcal{N}_\phi^T w_e da \tag{B.2g}$$

Within the Galerkin method, the field variables $\langle \tilde{\mathbf{w}} \rangle$ are approximated by the product of a set of basis functions $\mathcal{N}^i$ multiplying by the nodal variables $\langle \tilde{\mathbf{w}} \rangle^i$, the mechanical displacement field and electric potential are expressed as

$$\langle \tilde{\mathbf{u}} \rangle (\mathbf{x}) = \sum_{i=1}^{n} \mathcal{N}^i_u (\mathbf{x}) \begin{bmatrix} \langle \tilde{u}_x \rangle \\ \langle \tilde{u}_y \rangle \end{bmatrix}^i, \langle \tilde{\phi} \rangle (\mathbf{x}) = \sum_{i=1}^{n} \mathcal{N}^i_\phi (\mathbf{x}) \langle \tilde{\phi} \rangle^i \tag{B.3}$$

in which the superscript i corresponds to the ith node of the mesh, and n is the number of nodes of an element. Consequently, the operators in Eq. (B.2) at the ith node can be written by

$$\mathcal{N}^i_u = \begin{bmatrix} \mathcal{N}^i & 0 \\ 0 & \mathcal{N}^i \end{bmatrix}, \mathcal{N}^i_\phi = \mathcal{N}^i$$

$$\mathcal{B}^i_u = \begin{bmatrix} \frac{\partial \mathcal{N}^i}{\partial x} & 0 \\ 0 & \frac{\partial \mathcal{N}^i}{\partial y} \\ \frac{\partial \mathcal{N}^i}{\partial y} & \frac{\partial \mathcal{N}^i}{\partial x} \end{bmatrix}, \mathcal{B}^i_\phi = \begin{bmatrix} \frac{\partial \mathcal{N}^i}{\partial x} \\ \frac{\partial \mathcal{N}^i}{\partial y} \end{bmatrix}$$

Note that coupling tensors including $\bar{\mathbf{S}}$, $\bar{\mathbf{S}}^\dagger$, $\bar{\mathbf{W}}$, and $\bar{\mathbf{W}}^\dagger$ in Eq. (B.2) are available over the presence of Willis unit cells, and they are set to be zeros over normal structures.

References

[1] Z. Liu, X. Zhang, Y. Mao, Y.Y. Zhu, C.T.C. Z. Yang, P. Sheng, Locally resonant sonic materials, Science 289 (5485) (2000) 1734–1736.
[2] S.H. Lee, C.M. Park, Y.M. Seo, Z.G. Wang, C.K. Kim, Composite acoustic medium with simultaneously negative density and modulus, Phys. Rev. Lett. 104 (5) (2010) 054301.
[3] Y. Zhao, X.-X. Liu, A. Alù, Recent advances on optical metasurfaces, J. Opt. 16 (12) (2014) 123001.
[4] J.R. Willis, Effective constitutive relations for waves in composites and metamaterials, Proc. R. Soc. Lond. Ser. A Math. Phys. Eng. Sci. 467 (2131) (2011) 1865–1879.
[5] D.R. Smith, W.J. Padilla, D.C. Vier, S.C. Nemat-Nasser, S. Schultz, Composite medium with simultaneously negative permeability and permittivity, Phys. Rev. Lett. 84 (18) (2000) 4184–4187.
[6] M.B. Muhlestein, M.R. Haberman, A micromechanical approach for homogenization of elastic metamaterials with dynamic microstructure, Proc. R. Soc. A Math. Phys. Eng. Sciences 472 (2192) (2016) 20160438.
[7] A.N. Norris, A.L. Shuvalov, A.A. Kutsenko, Analytical formulation of three-dimensional dynamic homogenization for periodic elasticsystems, Proc. R. Soc. A Math. Phys. Eng. Sciences 468 (2142) (2012) 1629–1651.
[8] A. Alù, First-principles homogenization theory for periodic metamaterials, Phys. Rev. B 84 (7) (2011) 075153.
[9] J.R. Willis, Variational principles for dynamic problems for inhomogeneous elastic media, Wave Motion 3 (1) (1981) 1–11.
[10] J.R. Willis, The nonlocal influence of density variations in a composite, Int. J. Solids Struct. 21 (7) (1985) 805–817.
[11] J.R. Willis, Exact effective relations for dynamics of a laminated body, Mech. Mater. 41 (4) (2009) 385–393.
[12] H. Nassar, Q.-C. He, N. Auffray, Willis elastodynamic homogenization theory revisited for periodic media, J. Mech. Phys. Solids 77 (2015) 158–178.
[13] G.W. Milton, J.R. Willis, On modifications of Newton's second law and linear continuum elastodynamics, Proc. R. Soc. A Math. Phys. Eng. Sciences 463 (2079) (2007) 855–880.
[14] C.F. Sieck, A. Alù, M.R. Haberman, Origins of Willis coupling and acoustic bianisotropy in acoustic metamaterials through source-driven homogenization, Phys. Rev. B 96 (10) (2017) 104303.
[15] L. Quan, Y. Ra'di, D.L. Sounas, A. Alù, Maximum Willis coupling in acoustic scatterers, Phys. Rev. Lett. 120 (25) (2018) 254301.
[16] I. Lindell, A. Sihvola, S. Tretyakov, A.J. Viitanen, Electromagnetic Waves in Chiral and Bi-Isotropic Media, Artech House, Boston, 1994, pp. 1–22.
[17] M.V. Berry, The optical singularities of bianisotropic crystals, Proc. R. Soc. A Math. Phys. Eng. Sciences 461 (2059) (2005) 2071–2098.
[18] S. Nemat-Nasser, A. Srivastava, Overall dynamic properties of three-dimensional periodic elastic composites, Proc. R. Soc. Lond. Ser. A Math. Phys. Eng. Sci. 468 (2137) (2011) 269–287.
[19] A. Srivastava, Causality and passivity in elastodynamics, Proc. R. Soc. A Math. Phys. Eng. Sciences 471 (2180) (2015) 20150256.
[20] M.B. Muhlestein, C.F. Sieck, A. Alù, M.R. Haberman, Reciprocity, passivity and causality in Willis materials, Proc. R. Soc. A Math. Phys. Eng. Sciences 472 (2194) (2016) 20160604.
[21] G.W. Milton, D.J. Eyre, J.V. Mantese, Finite frequency range Kramers-Kronig relations: Bounds on the dispersion, Phys. Rev. Lett. 79 (16) (1997) 3062–3065.
[22] J.D. Achenbach, Reciprocity in Elastodynamics, in: Cambridge Monographs on Mechanics, Cambridge University Press, 2004.
[23] R. Pernas-Salomón, G. Shmuel, Symmetry breaking creates electro-momentum coupling in piezoelectric metamaterials, J. Mech. Phys. Solids 134 (2019) 10377.
[24] R. Pernas-Salomón, G. Shmuel, Fundamental principles for generalized Willis metamaterials, Phys. Rev. A 14 (6) (2020) 064005.
[25] R. Pernas-Salomón, M.R. Haberman, A.N. Norris, G. Shmuel, The electromomentum effect in piezoelectric Willis scatterers, Wave Motion 106 (2021) 102797.
[26] A. Muhafra, M. Kosta, D. Torrent, R. Pernas-Salomón, G. Shmuel, Homogenization of piezoelectric planar Willis materials undergoing antiplane shear, Wave Motion 108 (2022) 102833.
[27] J.-H. Lee, Z. Zhang, G.X. Gu, Maximum electro-momentum coupling in piezoelectric metamaterial scatterers, J. Appl. Phys. 132 (2022) 125108.
[28] M. Kosta, A. Muhafra, R. Pernas-Salomón, G. Shmuel, O. Amir, Maximizing the electromomentum coupling in piezoelectric laminates, Int. J. Solids Struct. 254–255 (2022) 111909.
[29] H. Nassar, X.C. Xu, A.N. Norris, G.L. Huang, Modulated phononic crystals: Non-reciprocal wave propagation and Willis materials, J. Mech. Phys. Solids 101 (2017) 10–29.
[30] Y.Y. Chen, X.P. Li, G.K. Hu, M.R. Haberman, G.L.G. Huang, An active mechanical Willis meta-layer with asymmetric polarizabilities, Nature Commun. 11 (2020) 3681.
[31] Y. Liu, Z. Liang, J. Zhu, L. Xia, O.M.-M.T. Brunet, A. Alù, J. Li, Willis metamaterial on a structured beam, Phys. Rev. X 9 (1) (2019) 011040.

[32] S. Nemat-Nasser, A. Srivastava, Overall dynamic constitutive relations of layered elastic composites, J. Mech. Phys. Solids 59 (10) (2011) 1953–1965.
[33] S.Y. Wang, K. Tai, Structural topology design optimization using Genetic Algorithms with a bit-array representation, Comput. Methods Appl. Mech. Engrg. 194 (36–38) (2005) 3749–3770.
[34] R. Christiansen, O. Sigmund, Compact 200 line MATLAB code for inverse design in photonics by topology optimization: tutorial, J. Opt. Soc. Amer. B 38 (2) (2021) 510–520.
[35] X.K. Han, Z. Zhang, Topological optimization of phononic crystal thin plate by a genetic algorithm, Sci. Rep. 9 (1) (2019) 8331.
[36] W. Hansel, A. Treptow, W. Becker, B. Freisleben, A heuristic and a genetic topology optimization algorithm for weight-minimal laminate structures, Compos. Struct. 58 (2) (2002) 287–294.
[37] G. Allaire, F. Jouve, A.-M. Toader, Structural optimization using sensitivity analysis and a level-set method, J. Comput. Phys. 194 (1) (2004) 363–393.